PCCP

ROYAL SOCIETY OF CHEMISTRY

PAPER

View Article Online
View Journal | View Issue

Cite this: *Phys. Chem. Chem. Phys.*, 2024, **26**, 24591

Fully quantal description of combined internal conversion and intersystem crossing processes in the smallest Criegee intermediate CH_2OO

Behnam Nikoobakht * and Horst Köppel

A quantal description of nuclear motion using coupled fifteen-state potential energy and spin–orbit coupling surfaces for studying the photodissociation of CH_2OO to $H_2CO(X^1A_1)$ + O^1D and $H_2CO(X^1A_1)$ + O^3P channels is presented. For the evaluation of surfaces, multireference electronic wave functions are employed. For the fully quantal description of the nuclear motion, we diabatize the PESs of the two and four lowest excited singlet and triplet states, respectively, within the three sets of vibronically coupled states, *i.e.* (B^1A', C^1A'), (a^3A', b^3A') and (a^3A'', b^3A''), employing the diabatization by ansatz method. This yields three different adiabatic-to-diabatic mixing angles, which are used for the diabatization of the spin–orbit coupling surfaces and allow to investigate simultaneously the internal conversion and intersystem crossing processes in CH_2OO using a nuclear quantum dynamical approach for the first time. Our calculation predicts the presence of a weak spectral band with irregular and discrete structures, which originates from the role of spin–orbit couplings. This band of the spectrum is mainly located between the minimum energy of the a^3A' state and the onset of the $B^1A' \leftarrow X^1A'$ spectral band. Furthermore, sizable SOC between the B^1A' and a^3A'' states mixes them *via* intersystem crossing. Due to the vibronic interaction between the a^3A'' and a^3A' states, the molecule finally relaxes to the a^3A' state and is dissociated to $H_2CO(X^1A_1)$ and O^3P products.

Received 22nd May 2024,
Accepted 22nd August 2024

DOI: 10.1039/d4cp02122c

rsc.li/pccp

1 Introduction

Internal conversion (IC) and intersystem crossing (ISC) are two important processes that are to be treated properly when studying theoretically the photochemistry of molecular systems.[1–7] The IC which is typically generated by an electronic degeneracy (*e.g.* conical intersection), drives a nonadiabatic process (*e.g.* IC) between two states with the same spin multiplicity.[8–11] In contrast, the ISC refers to a nonadiabatic process occurring between two electronic states with different spin multiplicities.[12,13]

If spin–orbit coupling (SOC) is present, when potential energy surfaces of the excited singlet and triplet states approach at the avoided crossing, there may be mixing of the singlet and triplet states at this point.[14] The spin–orbit interaction for polyatomic molecules is effective in promoting ISC close to the avoided crossing geometries only if (i) the orbital transition involved has the character of $p_x \rightarrow p_y$ orbital jump to induce orbital angular momentum and (ii) the orbital transition is localized on a single atom.[15]

For molecular systems including carbonyl groups (*e.g.* formaldehyde oxide), the possible ISC can take place between an initial state with $^1\pi\pi^*$ character and a final state with $^3n\pi^*$ character. For $^1\pi\pi^* \rightarrow {}^3n\pi^*$ transitions, some of the atomic orbitals have a one-center $p_y \rightarrow p_x$ spin–orbit coupling with the $^3n\pi^*$ state. As a result of that, a $^1\pi\pi^* \rightarrow {}^3n\pi^*$ transition is allowed.[16,17] This is known as the El-Sayed rule providing a selection rule for transitions from the singlet to the triplet states involving a change of orbital type.[16,17]

The dynamic simulation including IC and ISC requires PESs of the singlet and triplet states, vibronic coupling as well as SOC, which are generally computed by employing *ab initio* electronic structure methods. Incorporating the aforementioned electronic structure data for a fully quantal approach describing both IC and ISC for a specific molecule is not a trivial task. In order to achieve this task, we firstly diabatize separately each group of excited singlet and triplet states. In particular, diabatization is a crucial step for molecular systems when their PESs represent an avoided crossing in the adiabatic picture and are not smooth and slowly varying functions of the nuclear coordinates.[8,9,18,19] Thus, the diabatization provides a path way for understanding of nonadiabatic processes (*e.g.* IC) within the group of two states with smooth diagonal and off-diagonal elements of a potential Hamiltonian in the diabatic

Theoretische Chemie, Physikalisch-Chemisches Institut, Universität Heidelberg, INF 229, D-69120 Heidelberg, Germany. E-mail: behnam.nikoobakht@pci.uni-heidelberg.de; Fax: +49 6221 545221; Tel: +49 6221 545262

picture. Secondly, the SOC matrices as function of the nuclear coordinates are diabatized by using the adiabatic to diabatic (ATD) transformation evaluated in the previous step. The advantage of using PESs and SOC matrices in the diabatic picture is to remove not only the singular derivative couplings and discontinuities in PESs (owing to the presence of avoided crossings in the adiabatic picture) but also the discontinuities in SOCs as a function of the nuclear coordinates. As a result of the diabatization procedure, one obtains an analytical expression for the potential, in which the contributions of the vibronic coupling and SOC matrices are incorporated and, thus this provides a good starting point for the fully quantal description of the IC–ISC in a molecule.

The photodissociation dynamics of formaldehyde oxide can be considered as an example for studying the competition between the IC and ISC processes. Formaldehyde oxide possessing a carbonyl group for which the explicitly correlated multireference methods[20,21] (MRCI-F12b and RS2-F12) can be used for the evaluation of the PESs of the excited singlet and triplet states and SOCs.[22–26] Several investigations on the electronic structure of this molecule for the ground and excited states have been reported in the literature.[25,26] Excited state dynamics investigations focusing on the $B^1A' \leftarrow X^1A'$ absorption spectrum were reported, where only the vibronic coupling between the excited states was taken into account.[25,26] Due to limitations imposed by the potential consisting of only the excited singlet states and their vibronic coupling, one could explain the photodissociation of formaldehyde oxide *via* $CH_2OO(X^1A') \rightarrow H_2CO(X^1A_1) + O^1D$.[25–29] However, CH_2OO can be dissociated *via* $CH_2OO(X^1A') \rightarrow H_2CO(X^1A_1) + O^3P$ as well, which is energetically lower than the previous dissociation channel.[30,31] For a full quantum dynamic study of this channel, it is required to construct a model as indicated above, in which the PESs of the excited singlet and triplet states together with the vibronic coupling as well as SOC are incorporated. Due to lack of an accurate analytical representation of PESs data and SOCs in the diabatic representation, such a investigation relying on a fully quantal description of IC and ISC processes has not been reported comprehensively yet in the literature.[31] Investigation of these nonadiabatic processes and their roles for studying thoroughly the absorption spectroscopy in CH_2OO with considering the contributions of the relevant excited triplet states and SOCs constitutes the main research topic in the current manuscript. So far, the contributions of the excited singlet states have been treated for studying the absorption spectroscopy of this molecular system (see for instance ref. 25 and 26).

In this work, our aim is to build the diabatic representation for the PESs of the excited singlet and triplet states B^1A', C^1A', a^3A', b^3A', a^3A'' and b^3A'' and eventually diabatize the SOC between the excited singlet states and the triplet states. Within this unified diabatic representation, we carry out a nuclear quantum dynamics investigation which provides a theoretical basis for understanding the dissociation of CH_2OO in more detail.

2 Vibronic Hamiltonian

We use the vibronic Hamiltonian constructed in our previous work,[26] which has been already employed for studying the nonadiabatic dynamics of CH_2OO following the $B^1A' \leftarrow X^1A'$ electronic transition. The model was constructed using the adiabatic ground state X and the diabatic B and C excited states. In this work, we extent the model and include the relevant diabatic triplet states. In other words, the vibronic Hamiltonian $\boldsymbol{H}$ is constructed in the adiabatic state of X^1A' as well as diabatic states $a^{3+}A'$, $a^{30}A'$, $a^{3-}A'$, $b^{3+}A'$, $b^{30}A'$, $b^{3-}A'$, $a^{3+}A''$, $a^{30}A''$, $a^{3-}A''$, $b^{3+}A''$, $b^{30}A''$, $b^{3-}A''$, B^1A' and C^1A' (see *e.g.* ref. 8 and 9). The Hamiltonian

$$\boldsymbol{H} = T_N\mathbf{1} + \boldsymbol{W}(\boldsymbol{S}), \tag{1}$$

contains the kinetic part T_N ($\mathbf{1}$ stands for the 15×15 unit matrix), which is already computed in our previous work[26] by employing the the familiar G-matrix method of Wilson *et al.*[32,33] The potential part is $\boldsymbol{W}(\boldsymbol{S})$. In our previous work,[26] we consider the O–O and C–O stretching and the C–O–O bending modes, which are totally symmetric, with a′ symmetry for planar conformations (C_s point group). In the diabatic representation for the excited states, $\boldsymbol{W}(\boldsymbol{S})$ reads

$$\boldsymbol{W}(\boldsymbol{S}) = \begin{pmatrix}
V_X(\boldsymbol{S}) & 0 & 0 & 0 & 0 & 0 & 0 & 0 & 0 & 0 & 0 & 0 & 0 & 0 & 0 \\
0 & W^{+1}_{a'a'}(\boldsymbol{S}) & 0 & 0 & 0 & 0 & 0 & W_{a'b'}(\boldsymbol{S}) & W_{a'b'}(\boldsymbol{S}) & W_{a'b'}(\boldsymbol{S}) & 0 & 0 & 0 & 0 & 0 \\
0 & 0 & W^{0}_{a'a'}(\boldsymbol{S}) & 0 & 0 & 0 & 0 & W_{a'b'}(\boldsymbol{S}) & W_{a'b'}(\boldsymbol{S}) & W_{a'b'}(\boldsymbol{S}) & 0 & 0 & 0 & 0 & 0 \\
0 & 0 & 0 & W^{-1}_{a'a'}(\boldsymbol{S}) & 0 & 0 & 0 & W_{a'b'}(\boldsymbol{S}) & W_{a'b'}(\boldsymbol{S}) & W_{a'b'}(\boldsymbol{S}) & 0 & 0 & 0 & \mathrm{SOC}_a(\boldsymbol{S}) & \mathrm{SOC}_b(\boldsymbol{S}) \\
0 & 0 & 0 & 0 & W^{+1}_{a''a''}(\boldsymbol{S}) & 0 & 0 & 0 & 0 & 0 & W_{a''b''}(\boldsymbol{S}) & W_{a''b''}(\boldsymbol{S}) & W_{a''b''}(\boldsymbol{S}) & \mathrm{SOC}_c(\boldsymbol{S}) & \mathrm{SOC}_d(\boldsymbol{S}) \\
0 & 0 & 0 & 0 & 0 & W^{0}_{a''a''}(\boldsymbol{S}) & 0 & 0 & 0 & 0 & W_{a''b''}(\boldsymbol{S}) & W_{a''b''}(\boldsymbol{S}) & W_{a''b''}(\boldsymbol{S}) & \mathrm{SOC}_e(\boldsymbol{S}) & \mathrm{SOC}_f(\boldsymbol{S}) \\
0 & 0 & 0 & 0 & 0 & 0 & W^{-1}_{a''a''}(\boldsymbol{S}) & 0 & 0 & 0 & W_{a''b''}(\boldsymbol{S}) & W_{a''b''}(\boldsymbol{S}) & W_{a''b''}(\boldsymbol{S}) & 0 & 0 \\
0 & W_{a'b'}(\boldsymbol{S}) & W_{a'b'}(\boldsymbol{S}) & W_{a'b'}(\boldsymbol{S}) & 0 & 0 & 0 & W^{+1}_{b'b'}(\boldsymbol{S}) & 0 & 0 & 0 & 0 & 0 & 0 & 0 \\
0 & W_{a'b'}(\boldsymbol{S}) & W_{a'b'}(\boldsymbol{S}) & W_{a'b'}(\boldsymbol{S}) & 0 & 0 & 0 & 0 & W^{0}_{b'b'}(\boldsymbol{S}) & 0 & 0 & 0 & 0 & 0 & 0 \\
0 & W_{a'b'}(\boldsymbol{S}) & W_{a'b'}(\boldsymbol{S}) & W_{a'b'}(\boldsymbol{S}) & 0 & 0 & 0 & 0 & 0 & W^{-1}_{b'b'}(\boldsymbol{S}) & 0 & 0 & 0 & \mathrm{SOC}_g(\boldsymbol{S}) & \mathrm{SOC}_h(\boldsymbol{S}) \\
0 & 0 & 0 & 0 & W_{a''b''}(\boldsymbol{S}) & W_{a''b''}(\boldsymbol{S}) & W_{a''b''}(\boldsymbol{S}) & 0 & 0 & 0 & W^{+1}_{b''b''}(\boldsymbol{S}) & 0 & 0 & \mathrm{SOC}_i(\boldsymbol{S}) & \mathrm{SOC}_j(\boldsymbol{S}) \\
0 & 0 & 0 & 0 & W_{a''b''}(\boldsymbol{S}) & W_{a''b''}(\boldsymbol{S}) & W_{a''b''}(\boldsymbol{S}) & 0 & 0 & 0 & 0 & W^{0}_{b''b''}(\boldsymbol{S}) & 0 & \mathrm{SOC}_k(\boldsymbol{S}) & \mathrm{SOC}_l(\boldsymbol{S}) \\
0 & 0 & 0 & 0 & W_{a''b''}(\boldsymbol{S}) & W_{a''b''}(\boldsymbol{S}) & W_{a''b''}(\boldsymbol{S}) & 0 & 0 & 0 & 0 & 0 & W^{-1}_{b''b''}(\boldsymbol{S}) & 0 & 0 \\
0 & 0 & 0 & \mathrm{SOC}_a(\boldsymbol{S}) & \mathrm{SOC}_c(\boldsymbol{S}) & \mathrm{SOC}_e(\boldsymbol{S}) & 0 & 0 & 0 & \mathrm{SOC}_g(\boldsymbol{S}) & \mathrm{SOC}_i(\boldsymbol{S}) & \mathrm{SOC}_k(\boldsymbol{S}) & 0 & W_B(\boldsymbol{S}) & W_{BC}(\boldsymbol{S}) \\
0 & 0 & 0 & \mathrm{SOC}_b(\boldsymbol{S}) & \mathrm{SOC}_d(\boldsymbol{S}) & \mathrm{SOC}_f(\boldsymbol{S}) & 0 & 0 & 0 & \mathrm{SOC}_h(\boldsymbol{S}) & \mathrm{SOC}_j(\boldsymbol{S}) & \mathrm{SOC}_l(\boldsymbol{S}) & 0 & W_{BC}(\boldsymbol{S}) & W_C(\boldsymbol{S})
\end{pmatrix} \tag{2}$$

In eqn (2), the vector $\boldsymbol{S}$ refers to the relevant internal coordinates, O–O and C–O stretch and C–O–O bend for our present purposes. Furthermore, the diagonal elements refer to

the PESs of the adiabatic state X^1A' as well as diabatic states $a^{3+}A'$, $a^{30}A'$, $a^{3-}A'$, $b^{3+}A'$, $b^{30}A'$, $b^{3-}A'$, $a^{3+}A''$, $a^{30}A''$, $a^{3-}A''$, $b^{3+}A''$, $b^{30}A''$, $b^{3-}A''$, B^1A' and C^1A'. The off-diagonal elements $SOC_a(\boldsymbol{S})$, $SOC_c(\boldsymbol{S})$, $SOC_e(\boldsymbol{S})$, $SOC_g(\boldsymbol{S})$ and $SOC_i(\boldsymbol{S})$ are the spin–orbit coupling (SOC) between the B^1A' and the $a^{3-}A'$, $a^{3+}A''$, $a^{30}A''$, $b^{3-}A'$, $b^{3+}A''$ and $b^{30}A''$ states, respectively. The off-diagonal elements $SOC_b(\boldsymbol{S})$, $SOC_d(\boldsymbol{S})$, $SOC_f(\boldsymbol{S})$, $SOC_h(\boldsymbol{S})$, $SOC_j(\boldsymbol{S})$ and $SOC_l(\boldsymbol{S})$ are the SOC matrix elements between the C^1A' and the $a^{3-}A'$, $a^{3+}A''$, $a^{30}A''$, $b^{3-}A'$, $b^{3+}A''$ and $b^{30}A''$ states, respectively. The notation SOC in eqn (2) stands for the spin–orbit coupling matrix elements.

In eqn (2), $W_{BC}(\boldsymbol{S})$, $W_{a'b'}(\boldsymbol{S})$ and $W_{a''b''}(\boldsymbol{S})$ are the vibronic coupling terms between the pairs of coupled states (B^1A',C^1A'), (a^3A',b^3A') and (a^3A'',b^3A''), respectively. The numerical values for the coupling constants W_{BC}, $W_{a'b'}$ and $W_{a''b''}$ are 0.049 eV, 0.1 eV and 0.1 eV, respectively (see below for the detailed information regarding the method of calculation). The vibronic coupling constants are computed as the minimum energy difference of the lower and upper potential energy curves along R_{OO} at the avoided crossing geometries (shown in Fig. 3). As can be seen, they are in the excitation energy range of the singlet and triplet transitions relevant to the absorption spectrum. As a result, these avoided crossing shown in in Fig. 3 are relevant in our quantum dynamical calculations. We compute these vibronic coupling by taking the matrix elements to be simple analytical functions of the coordinates, for example, taking the off-diagonal element of the coupling matrix **W** as constant and the diagonal elements as linear functions of the coordinates[25,26] (see eqn (2)). However, in a higher-dimensional treatment, vibronic coupling constants are not taken globally as constant, but rather the minimum energy difference is determined separately for different angles θ_{COO} ($90 < \theta_{COO} < 180$) and r_{CO} ($1.12 < r_{CO} < 1.32$). Detailed information regarding the evaluations of the vibronic coupling constants was given in our previous work[25,26] and we thus skip it here. We should mention that the vibronic coupling of the C state with higher excited singlet states is not treated in the current work, because the energy at their avoided crossing is relatively high and thus its influence on the dynamics may not be important.

As will be explained below, the ISC process happens more likely in the vicinity of the avoided crossing geometries. Thus, we consider the SOC matrices at the minimum energy gaps between the singlet B and C states with the relevant triplet states and average this over the O–O, C–O–O and C–O coordinates in our nuclear quantum dynamical calculation. More details regarding the average values of SOC matrices at the minimum energy gaps will be provided in Section 4, (see also Fig. 12 and 13).

3 Diabatization by ansatz

3.1 Diabatization of excited state PESs

For the purpose of carrying out the nuclear quantum dynamical calculation, we need to diabatize the PESs computed in the adiabatic picture in the first place. For this task, we use a so-called diabatization-by-ansatz method, which is well described in the literature.[8,9] As indicated, the singlet and triplet electronic states a^3A', b^3A', a^3A'', b^3A'', B^1A' and C^1A' are involved in the dynamics. Thus, we need to diabatize the PESs corresponding to these states. For this task, we diabatize these states considering three different blocks in the Hamiltonian model (by employing the diabatization-by-ansatz method). The first block involves the a^3A', b^3A' states, while the second block includes the a^3A'' and b^3A'' states. The two singlet B and C states constitute the third block.

Diagonalizing blocks of the potential matrix in eqn (2) results in the energies of the a^3A', b^3A', a^3A'', b^3A'' B^1A' and C^1A' states in the adiabatic picture. The diagonalization of each block can be represented as follows:

$$\boldsymbol{U}_{ij}(\boldsymbol{S})^{\dagger}\begin{pmatrix} W_i(\boldsymbol{S}) & W_{ij}(\boldsymbol{S}) \\ W_{ij}(\boldsymbol{S}) & W_j(\boldsymbol{S}) \end{pmatrix}\boldsymbol{U}_{ij}(\boldsymbol{S}) = \begin{pmatrix} V_i(\boldsymbol{S}) & 0 \\ 0 & V_j(\boldsymbol{S}) \end{pmatrix}, \quad (3)$$

where $i \in \{a^3A', a^3A'', B^1A'\}$ and $j \in \{b^3A', b^3A'', C^1A'\}$. The off-diagonal term $W_{ij}(\boldsymbol{S})$ refers to the vibronic coupling between the coupled states (a^3A',b^3A'), (a^3A'',b^3A'') and (B^1A',C^1A') which are shown as $W_{a'b'}(\boldsymbol{S})$, $W_{a''b''}(\boldsymbol{S})$ and $W_{BC}(\boldsymbol{S})$, respectively, in the Hamiltonian model. In this equation, $\boldsymbol{U}_{ij}(\boldsymbol{S})$ is a unitary transformation and reads

$$\boldsymbol{U}(\boldsymbol{S}) = \begin{pmatrix} U_{ii}(\boldsymbol{S}) & U_{ij}(\boldsymbol{S}) \\ U_{ji}(\boldsymbol{S}) & U_{jj}(\boldsymbol{S}) \end{pmatrix} = \begin{pmatrix} \cos(\alpha_{ij}(\boldsymbol{S})) & \sin(\alpha_{ij}(\boldsymbol{S})) \\ -\sin(\alpha_{ij}(\boldsymbol{S})) & \cos(\alpha_{ij}(\boldsymbol{S})) \end{pmatrix}, \quad (4)$$

where $\alpha(\boldsymbol{S})$ is the adiabatic to diabatic (ATD) transformation angle and given by

$$\alpha_{ij}(\boldsymbol{S}) = \frac{1}{2}\arctan\frac{2W_{ij}(\boldsymbol{S})}{W_i(\boldsymbol{S}) - W_j(\boldsymbol{S})}. \quad (5)$$

We define the matrix elements of the unitary transformation using the sin and cosine functions depending on the ATD angle (see eqn (4) and (5)). However, we can also get explicit expressions for the matrix elements of the unitary transformation in eqn (4) in terms of PESs of the excited state directly rather than using trigonometric functions.[34] In other words, the matrix elements of the unitary transformation $\boldsymbol{U}$ can be evaluated in terms of $W_i(\boldsymbol{S})$, $W_j(\boldsymbol{S})$, $W_{ij}(\boldsymbol{S})$, $V_i(\boldsymbol{S})$ and $V_j(\boldsymbol{S})$, (where indexes i and j are defined above) as follows,

$$\begin{aligned} U_{ii}(\boldsymbol{S}) &= \frac{1}{\sqrt{1+x_i^2(\boldsymbol{S})}} \quad U_{ji}(\boldsymbol{S}) = \frac{-x_i(\boldsymbol{S})}{\sqrt{1+x_i^2(\boldsymbol{S})}} \\ U_{ij}(\boldsymbol{S}) &= \frac{-x_j(\boldsymbol{S})}{\sqrt{1+x_j^2(\boldsymbol{S})}} \quad U_{jj}(\boldsymbol{S}) = \frac{1}{\sqrt{1+x_j^2(\boldsymbol{S})}}, \end{aligned} \quad (6)$$

where, $x_i(\boldsymbol{S})$ and $x_j(\boldsymbol{S})$ read

$$\begin{aligned} x_i(\boldsymbol{S}) &= \frac{W_i(\boldsymbol{S}) - V_i(\boldsymbol{S})}{W_{ij}(\boldsymbol{S})} \\ x_j(\boldsymbol{S}) &= \frac{W_j(\boldsymbol{S}) - V_j(\boldsymbol{S})}{W_{ij}(\boldsymbol{S})}. \end{aligned} \quad (7)$$

Taking the eigenvalue problem in eqn (3) to be solved, we

compute the diabatic PESs in terms of adiabatic energies $V_i(\boldsymbol{S})$ and $V_j(\boldsymbol{S})$ obtained from the electronic structure methods discussed in the previous section. Thus, the diabatized surfaces can be computed using the following relations,

$$\begin{aligned} W_i(\boldsymbol{S}) &= \frac{V_i(\boldsymbol{S})+V_j(\boldsymbol{S})}{2} - \sqrt{\left(\frac{V_i(\boldsymbol{S})-V_j(\boldsymbol{S})}{2}\right)^2 - W_{ij}^2} \\ W_j(\boldsymbol{S}) &= \frac{V_i(\boldsymbol{S})+V_j(\boldsymbol{S})}{2} + \sqrt{\left(\frac{V_i(\boldsymbol{S})-V_j(\boldsymbol{S})}{2}\right)^2 - W_{ij}^2}. \end{aligned} \tag{8}$$

Here W_{ij} is computed as the minimum energy difference between the j and i states along R_{OO}, as referred in Section 2 and detailed in ref. 25 and 26.

3.2 Diabatization of SOC matrix elements

As mentioned in the previous section, the three sets of (B^1A',C^1A'), (a^3A',b^3A') and (a^3A'',b^3A'') are diabatized by using eqn (3) and (8). This diabatization results in the three separate ATD transformation angles as given in eqn (5). We used these ATD transformation angles and diabatize the SOC matrix elements as described in the following. For the sake of simplicity, we use the three angles α_1, α_2 and α_3 for the representation of the ATD transformation angles in the three sets of (B^1A',C^1A'), (a^3A',b^3A') and (a^3A'',b^3A''), respectively, instead of using the two index notations (ij) as used in eqn (5).

For the three sets of (B^1A',C^1A'), (a^3A',b^3A') and (a^3A'',b^3A''), the ATD transformations from the adiabatic to the diabatic picture for each ATD transformation angle can be written as rotation matrices

$$\begin{pmatrix} |B^1A'^{(d)}\rangle \\ |C^1A'^{(d)}\rangle \end{pmatrix} = \begin{pmatrix} \cos\alpha_1 & -\sin\alpha_1 \\ \sin\alpha_1 & \cos\alpha_1 \end{pmatrix} \begin{pmatrix} |B^1A'\rangle \\ |C^1A'\rangle \end{pmatrix} \tag{9}$$

$$\begin{pmatrix} |a^3A'^{(d)}\rangle \\ |b^3A'^{(d)}\rangle \end{pmatrix} = \begin{pmatrix} \cos\alpha_2 & -\sin\alpha_2 \\ \sin\alpha_2 & \cos\alpha_2 \end{pmatrix} \begin{pmatrix} |a^3A'\rangle \\ |b^3A'\rangle \end{pmatrix} \tag{10}$$

$$\begin{pmatrix} |a^3A''^{(d)}\rangle \\ |b^3A''^{(d)}\rangle \end{pmatrix} = \begin{pmatrix} \cos\alpha_3 & -\sin\alpha_3 \\ \sin\alpha_3 & \cos\alpha_3 \end{pmatrix} \begin{pmatrix} |a^3A''\rangle \\ |b^3A''\rangle \end{pmatrix} \tag{11}$$

Inserting the diabatic states obtained from eqn (9)–(11) into the SOC matrix elements results in the diabatized SOC matrix elements between the singlet states B^1A', C^1A' and the triplet states a^3A', b^3A', a^3A'', b^3A'',

$$\begin{aligned} \left\langle B^1A'^{(d)}|H_{SO}|b^{3\pm,0}A'^{(d)}\right\rangle &= \cos\alpha_1\sin\alpha_2\langle B^1A'|H_{SO}|a^{3\pm,0}A'\rangle \\ &+ \cos\alpha_1\cos\alpha_2\langle B^1A'|H_{SO}|b^{3\pm,0}A'\rangle \\ &- \sin\alpha_1\sin\alpha_2\langle C^1A'|H_{SO}|a^{3\pm,0}A'\rangle \\ &- \sin\alpha_1\cos\alpha_2\langle C^1A'|H_{SO}|b^{3\pm,0}A'\rangle \end{aligned} \tag{12}$$

$$\begin{aligned} \left\langle B^1A'^{(d)}|H_{SO}|a^{3\pm,0}A'^{(d)}\right\rangle &= \cos\alpha_1\cos\alpha_2\langle B^1A'|H_{SO}|a^{3\pm,0}A'\rangle \\ &- \cos\alpha_1\sin\alpha_2\langle B^1A'|H_{SO}|b^{3\pm,0}A'\rangle \\ &- \sin\alpha_1\cos\alpha_2\langle C^1A'|H_{SO}|a^{3\pm,0}A'\rangle \\ &+ \sin\alpha_1\sin\alpha_2\langle C^1A'|H_{SO}|b^{3\pm,0}A'\rangle \end{aligned} \tag{13}$$

$$\begin{aligned} \left\langle B^1A'^{(d)}|H_{SO}|b^{3\pm,0}A''^{(d)}\right\rangle &= \cos\alpha_1\sin\alpha_3\langle B^1A'|H_{SO}|a^{3\pm,0}A''\rangle \\ &+ \cos\alpha_1\cos\alpha_3\langle B^1A'|H_{SO}|b^{3\pm,0}A''\rangle \\ &- \sin\alpha_1\sin\alpha_3\langle C^1A'|H_{SO}|a^{3\pm,0}A''\rangle \\ &- \sin\alpha_1\cos\alpha_3\langle C^1A'|H_{SO}|b^{3\pm,0}A''\rangle \end{aligned} \tag{14}$$

$$\begin{aligned} \left\langle B^1A'^{(d)}|H_{SO}|a^{3\pm,0}A''^{(d)}\right\rangle &= \cos\alpha_1\cos\alpha_3\langle B^1A'|H_{SO}|a^{3\pm,0}A''\rangle \\ &- \cos\alpha_1\sin\alpha_3\langle B^1A'|H_{SO}|b^{3\pm,0}A''\rangle \\ &- \sin\alpha_1\cos\alpha_3\langle C^1A'|H_{SO}|a^{3\pm,0}A''\rangle \\ &+ \sin\alpha_1\sin\alpha_3\langle C^1A'|H_{SO}|b^{3\pm,0}A''\rangle \end{aligned} \tag{15}$$

$$\begin{aligned} \left\langle C^1A'^{(d)}|H_{SO}|b^{3\pm,0}A'^{(d)}\right\rangle &= \sin\alpha_1\sin\alpha_2\langle B^1A'|H_{SO}|a^{3\pm,0}A'\rangle \\ &+ \sin\alpha_1\cos\alpha_2\langle B^1A'|H_{SO}|b^{3\pm,0}A'\rangle \\ &+ \cos\alpha_1\sin\alpha_2\langle C^1A'|H_{SO}|a^{3\pm,0}A'\rangle \\ &+ \cos\alpha_1\cos\alpha_2\langle C^1A'|H_{SO}|b^{3\pm,0}A'\rangle \end{aligned} \tag{16}$$

$$\begin{aligned} \left\langle C^1A'^{(d)}|H_{SO}|a^{3\pm,0}A'^{(d)}\right\rangle &= \sin\alpha_1\cos\alpha_2\langle B^1A'|H_{SO}|a^{3\pm,0}A'\rangle \\ &- \sin\alpha_1\sin\alpha_2\langle B^1A'|H_{SO}|b^{3\pm,0}A'\rangle \\ &+ \cos\alpha_1\cos\alpha_2\langle C^1A'|H_{SO}|a^{3\pm,0}A'\rangle \\ &- \cos\alpha_1\sin\alpha_2\langle C^1A'|H_{SO}|b^{3\pm,0}A'\rangle \end{aligned} \tag{17}$$

$$\begin{aligned} \left\langle C^1A'^{(d)}|H_{SO}|b^{3\pm,0}A''^{(d)}\right\rangle &= \sin\alpha_1\sin\alpha_3\langle B^1A'|H_{SO}|a^{3\pm,0}A''\rangle \\ &+ \sin\alpha_1\cos\alpha_3\langle B^1A'|H_{SO}|b^{3\pm,0}A''\rangle \\ &+ \cos\alpha_1\sin\alpha_3\langle C^1A'|H_{SO}|a^{3\pm,0}A''\rangle \\ &+ \cos\alpha_1\cos\alpha_3\langle C^1A'|H_{SO}|b^{3\pm,0}A''\rangle \end{aligned} \tag{18}$$

$$\left\langle C^1A'^{(d)}|H_{SO}|a^{3\pm,0}A''^{(d)}\right\rangle = \sin\alpha_1\cos\alpha_3\langle B^1A'|H_{SO}|a^{3\pm,0}A''\rangle + \cos\alpha_1\cos\alpha_3\langle C^1A'|H_{SO}|a^{3\pm,0}A''\rangle - \sin\alpha_1\sin\alpha_3\langle B^1A'|H_{SO}|b^{3\pm,0}A''\rangle - \cos\alpha_1\sin\alpha_3\langle C^1A'|H_{SO}|b^{3\pm,0}A''\rangle. \quad (19)$$

As mentioned in Section 3.1, the matrix elements of the unitary transformation of eqn (4) can be defined in terms of the diabatic and adiabatic PESs (see eqn (6) and (7)). Thus, for the purpose of the evaluations of the SOC in the diabatic picture using eqn (12)–(19), we will use eqn (6) and (7) to compute the sin and cosine functions mentioned in eqn (12)–(19) and eventually calculate the SOC matrix elements in the diabatic picture. In Fig. 5, 6 and 7, the matrix elements of the unitary transformation of eqn (4) (or eigenvectors) for the three sets of states (B^1A',C^1A'), (a^3A',b^3A') and (a^3A'',b^3A'') are shown.

Inserting the unitary transformations of eqn (6) and (7) into eqn (12)–(19) results in the SOC matrix elements in the diabatic representation as function of R_{OO} stretching coordinate shown in Fig. 8–11 (shown by dashed lines). Comparing the diabatized SOC curves with their corresponding version in the adiabatic representation reveals that the diabatization procedure removes the zig-zag features of SOC curves in the adiabatic representation and instead creates smooth SOC curves in the diabatic representation (as shown by dashed lines in Fig. 8–11). As a result, the diabatization procedure is able to generate SOC curves, which are slowly varying functions of the nuclear coordinates as also observed in the case of PESs of the relevant excited states (see Fig. 4).

4 Quantum chemistry results

For our electronic structure calculations, we use the ground state electronic structure of CH_2OO taken from our previous work,[25] where the UCCSD(T)-F12b/cc-pVTZ-F12 level of theory[35,36] imposing planarity (C_s point group) was employed (see Fig. 1). For the evaluation of the excited state potential energy surfaces (PESs), we use the CASPT2-F12 (hereafter RS2-F12)[21] methods employing the cc-pVTZ-F12 basis set for all atoms.[36] We employ the full-valence complete active space (CAS), with 18 electrons distributed in 14 orbitals (18e,14o) as already used in our previous works.[25,26] In the current work, the PESs along the O–O and C–O stretching as well as C–O–O bending modes for the four triplet states a^3A', b^3A', a^3A'' and b^3A'' are computed. The 3D PESs of the singlet states X^1A', B^1A', C^1A' along r_{OO}, r_{CO} and θ_{COO} were computed in our previous work.[26] The PESs are computed in the range $1.09 < r_{OO} < 4$, $1.12 < r_{CO} < 1.32$ and $92^\circ < \theta_{COO} < 120^\circ$. The intervals between adjacent points along r_{OO}, r_{CO} and θ_{COO} are 0.05, 0.05 and 2°, respectively. For the evaluation of PESs along the relevant coordinates, we keep the other coordinates fixed at the equilibrium values at the ground state obtained in our previous work[25] and shown in Fig. 1. In total, we compute 4720 points for the construction of the PESs for each triplet state using the RS2-F12 method. Spin–orbit couplings (SOCs) among the aforementioned singlet and triplet states along the O–O and C–O stretching as well as C–O–O bending modes are computed by employing the MRCI wavefunction. In this calculation, we consider absolute values of SOCs. However, we should mention that this is an approximation and more accurate way regarding adjusting the signs of wavefunctions can be found in ref. 37. For this calculation, the same active space is employed as used for the evaluation of the PESs. However, the extension F12 from the aforementioned basis set for all atoms is dropped as we use the MRCI wavefunction in this case. For MRCI wavefunctions,

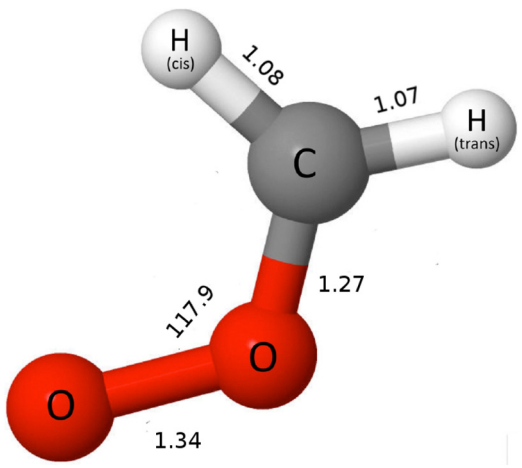

Fig. 1 The ground state equilibrium structure of CH_2OO.[25] The bond length and bond angle are given in angstrom and degrees, respectively.

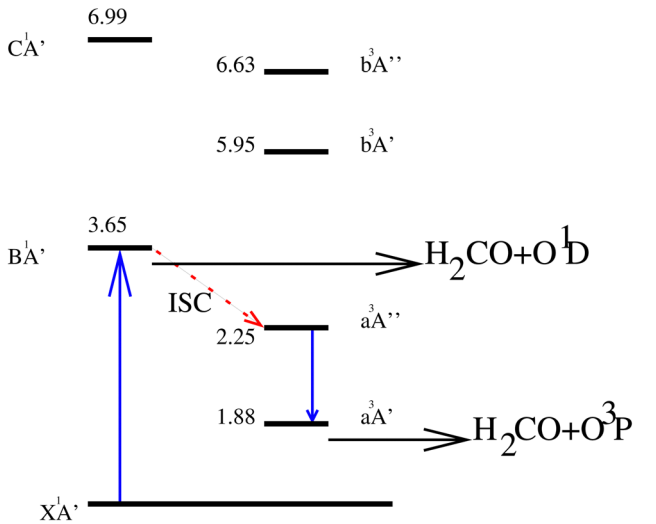

Fig. 2 Pictorial representation of the vertical excitation energies of the singlet and triplet states of CH_2OO computed using the RS2-F12 method. The different dissociation channels are shown. UV absorption excites CH_2OO from its ground to the excited B states resulting in photodissociation the products $H_2CO(X)$ and O^1D. The other dissociation channel (energetically lower than the first one) occurs through the ISC between B^1A' and a^3A'' as well as the vibronic coupling between the a^3A'' and a^3A' leading to the products $H_2CO(X)$ and O^3P.

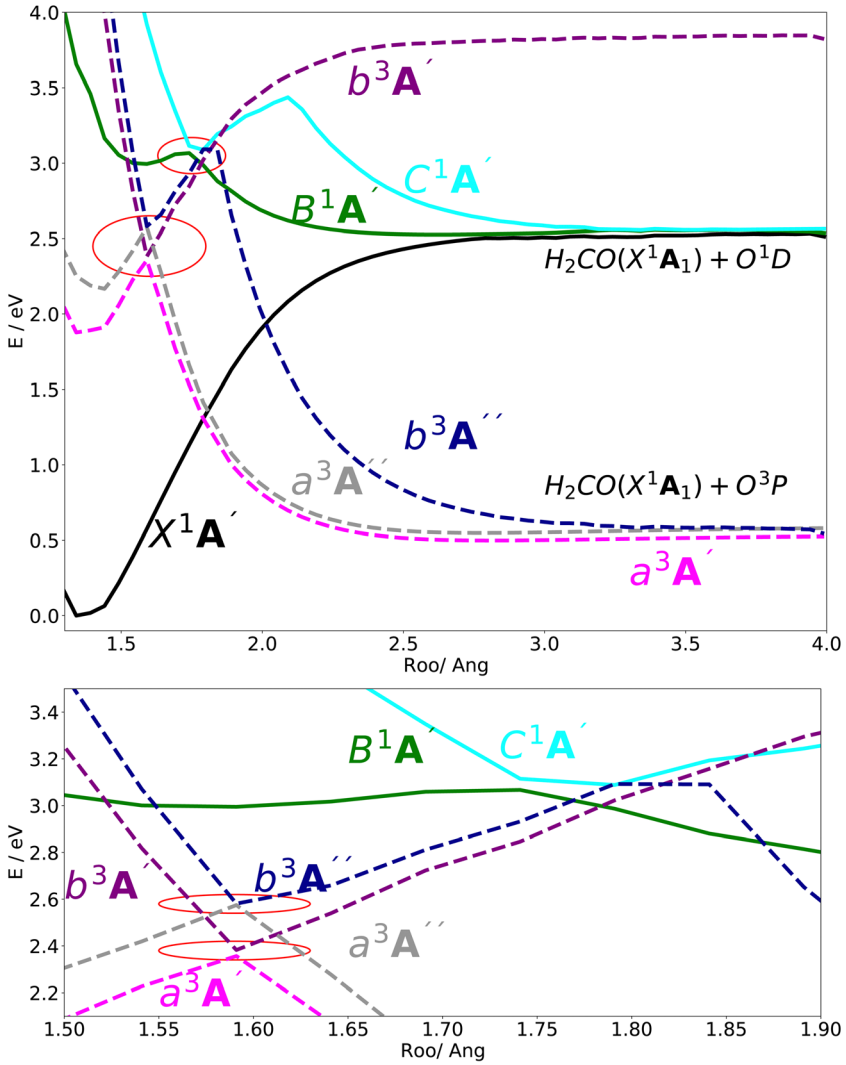

Fig. 3 (upper) The adiabatic PE curves along the OO stretching mode for the X^1A', B^1A', C^1A', a^3A', b^3A', a^3A'' and b^3A'' states. (lower) The adiabatic PE curves along O–O stretching mode, zooming in geometries in the range $1.55 < R_{OO} < 1.80$ (indicated by red circles in the upper panel). The bonding angle θ_{COO} and the stretching mode R_{CO} are fixed at the equilibrium structure values 117.905° and 1.27, respectively.

the full Breit–Pauli operator is employed for evaluating the spin–orbit matrix elements between internal configurations (no electrons in external orbitals), while for contributions of external configurations a mean-field one-electron fock operator is employed (see ref. 38 for more information). The electronic structure calculations are carried out by using the MOLPRO 2019.2 suite of programs.[39]

In Fig. 2, the vertical excitation energies of the excited singlet and triplet states are depicted and shown in ascending order. In the upper panel of Fig. 3, the adiabatic PE curves along the O–O stretching mode for X^1A', a^3A', b^3A', a^3A'', b^3A'', B^1A' and C^1A' are presented (based on the ordering of the diabatic basis introduced in eqn (3)). For this PE cut, the stretching mode O–O is varied within the range shown in Fig. 3 and the other bond lengths and angles are kept at the equilibrium structure values as shown partly in Fig. 1. In this figure, the PE curves of excited singlet states are shown by solid lines while the PE curves for the excited triplet states are shown by dashed lines. From this figure, one can see several avoided crossings between the PE curves of the excited singlet and triplet states with the same symmetry. As inferred from the lower panel of Fig. 3, the avoided crossings occur between the two singlet states B^1A' and C^1A' at 3.06 eV with R_{OO} = 1.741, between the excited triplet states a^3A' and b^3A' at 2.35 eV with R_{OO} = 1.591 and finally between the excited triplet states a^3A'' and b^3A'' at 2.57 eV with R_{OO} = 1.591. SOCs along the O–O stretching mode in the adiabatic representation are presented in Fig. 8–11. All SOC matrix elements in the adiabatic representation are shown by gray and green solid lines in these figures. We compute the SOCs among the singlet B and C states with the a^3A', b^3A', a^3A'' and b^3A'' states for different spin components 0, ±1.

The dissociation channel along the O–O stretching coordinate after excitation to the B state leads to the $H_2CO(X^1A_1)$ and O^1D products. The electronic states X^1A', B^1A' and C^1A' correlate with this same asymptotic limit generating the $H_2CO(X^1A_1)$

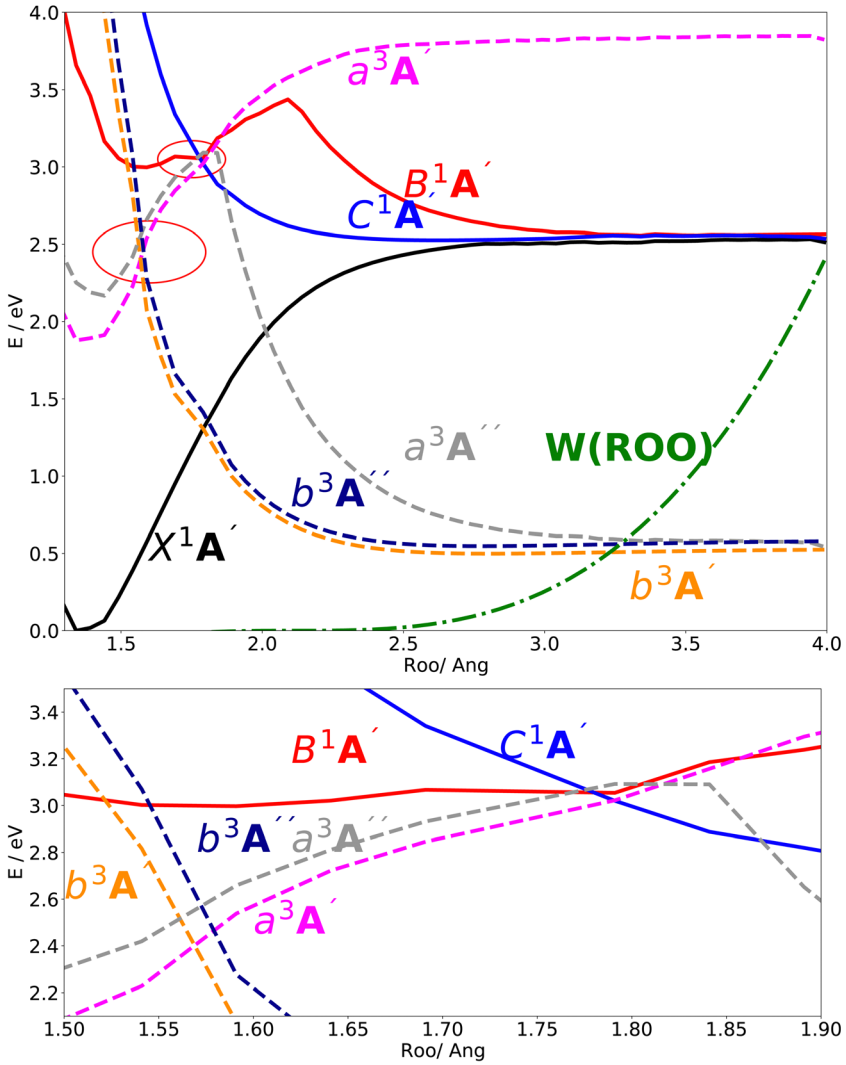

Fig. 4 (upper) The diabatic PE curves along the OO stretching mode for the X^1A', B^1A', C^1A', a^3A', b^3A', a^3A'' and b^3A'' states. The CAP is included as the dashed-dotted green curve. (lower) The diabatic PE curves along O–O stretching mode, zooming in geometries in the range $1.55 < R_{OO} < 1.80$ (indicated by red circles in the upper panel).

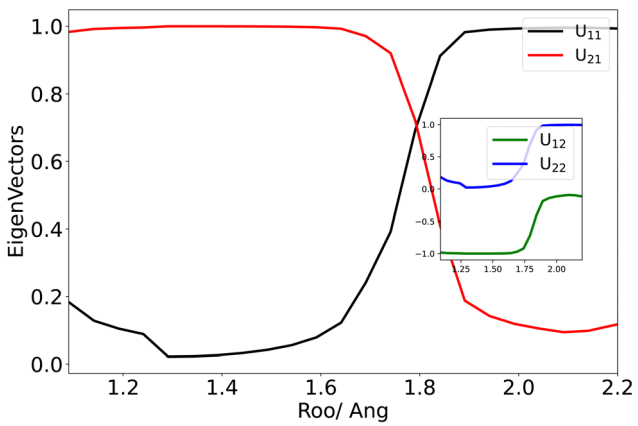

Fig. 5 The eigenvectors or the unitary transformation matrix elements obtained from the diabatization of the B^1A' and C^1A' states.

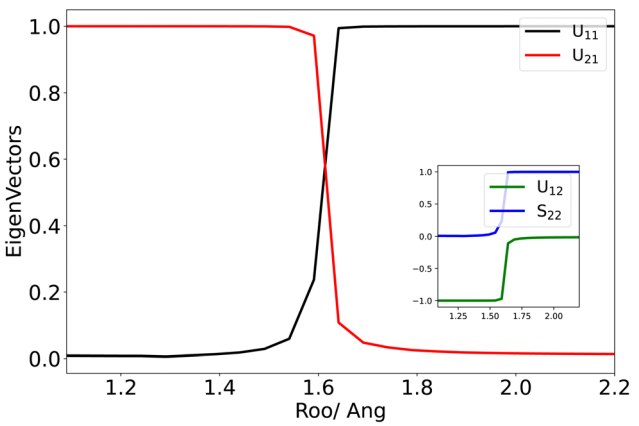

Fig. 6 The eigenvectors or the unitary transformation matrix elements obtained from the diabatization of the a^3A' and b^3A' states.

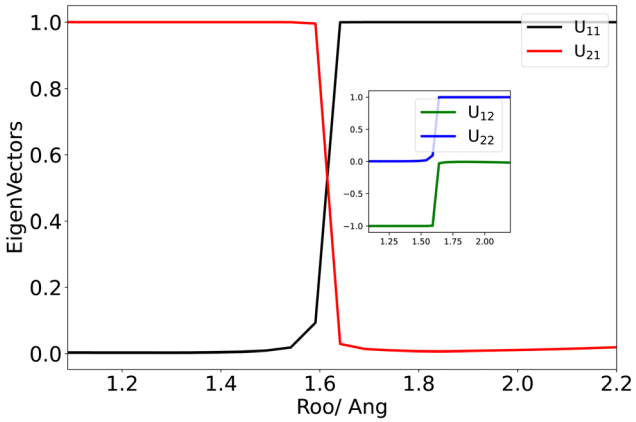

Fig. 7 The eigenvectors or the unitary transformation matrix elements obtained from the diabatization of the a^3A'' and b^3A'' states.

and O^1D products (see upper panel of Fig. 3). The dissociation energy corresponds for this channel is estimated $\approx$57 kcal mol^{-1} or 2.47 eV, which is in close agreement with the experimental value $\approx$54 kcal mol^{-1} or 2.34 eV.[40] As can be seen in the upper panel of Fig. 3, the three triplet states a^3A', a^3A'' and b^3A'' correlate adiabatically with the same state in the asymptotic O–O stretching range and this represents a dissociation channel, which is energetically lower than the aforementioned dissociation channel. In this new channel, $CH_2OO(X^1A')$ is dissociated into $H_2CO(X^1A_1)$ and O^3P products. Based on our calculation, the dissociation energy corresponding to this channel is estimated $\approx$13 kcal mol^{-1} or 0.56 eV.

Since the 3D PESs and SOCs matrix elements are inherently computed in the adiabatic picture within the electronic structure formalism, we need to diabatize them for the nuclear quantum dynamics purposes. Hence, we diabatize the 3D excited PESs and SOCs matrix elements using the method explained in Sections 3.1 and 3.2. The diabatic PE curves along the relevant singlet and triplet states are shown in the upper panel of Fig. 4 and the new features of the crossing (in contrast to the adiabatic picture) among the excited states PESs are shown in the lower panel of Fig. 4. The diabatized SOC matrix elements are computed using the method explained in Section 3.2 and are shown by red and blue dashed lines in Fig. 8–11. Due to the diabatization process, the PESs and SOC matrix elements become often smooth and slowly varying functions of the nuclear coordinates which does not hold for the adiabatic and SOC matrix elements. As shown below, the SOC matrix elements along O–O stretching coordinate have large values below $\sim$2, where the energy gaps between PESs of the singlet and triplet states are minimum, *i.e.* the ISC process can more likely happen there (see Fig. 12 and 13). Thus, we plot the SOC matrix elements along O–O stretching coordinate until 2. In Table 1, the minimum energies and barrier heights for the diabatic B^1A' and a^3–A'' states are shown.

In the panels of Fig. 12a and b, the contour plots of the energy differences between the 2D PESs for the (B^1A', a^3A'') and (C^1A', a^3A'') are depicted. In the panels of Fig. 12c and d, the sizes of SOC matrix elements at the geometries, where the energy gap between the (B^1A', a^3A'') and (C^1A', a^3A'') are minimum, are depicted. In Fig. 12a, the small energy gap in the range of $1.40 < R_{OO} < 1.85$ is in the range of 0–0.6 eV. Fig. 12c reveals that the size of SOCs in the range of $1.56 < R_{OO} < 1.64$ and $100 \leq \theta_{COO} \leq 120$ has the average value of 5×10^{-3} eV (or 42 cm^{-1}). This small energy gap between the PESs of the B^1A', a^3A'' states and the relatively strong SOC between them (within the range of $1.50 < R_{OO} < 1.60$ and $100 \leq \theta_{COO} \leq 120$) leads an efficient intersystem crossing (ISC).

In Fig. 12b, within the range $1.60 < R_{OO} < 1.70$, there is an energy gap of 0.5–1.5 eV between the PESs of the C^1A'

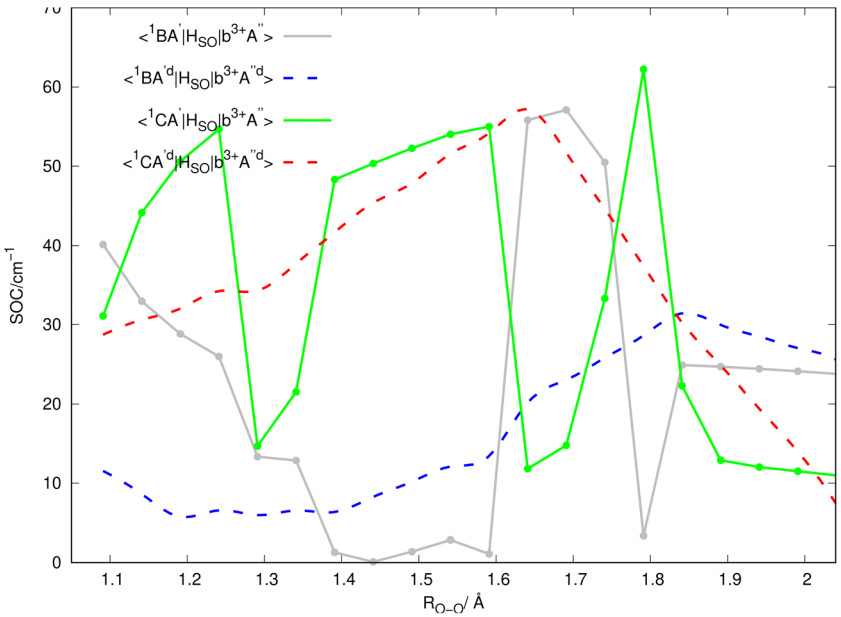

Fig. 8 SOC matrix elements (shown in the caption of the figure) in the adiabatic (solid lines) and diabatic (dashed lines) representations.

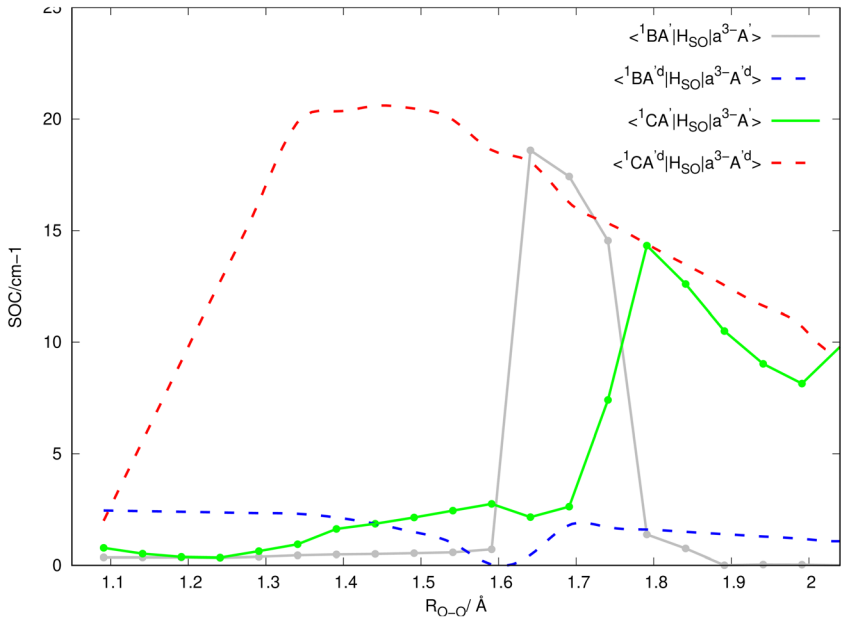

Fig. 9 SOC matrix elements (shown in the caption of the figure) in the adiabatic (solid lines) and diabatic (dashed lines) representations.

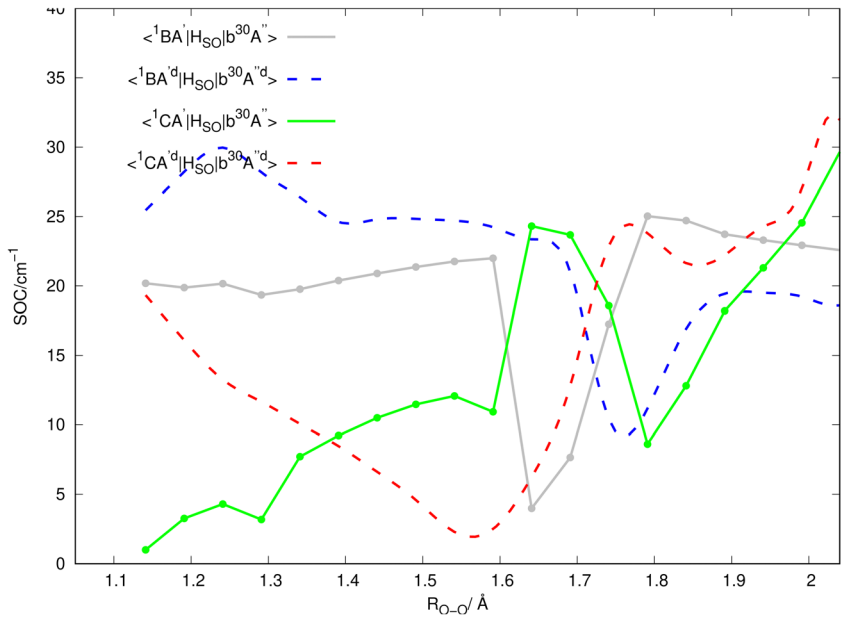

Fig. 10 SOC matrix elements (shown in the caption of the figure) in the adiabatic (solid lines) and diabatic (dashed lines) representations.

and a^3A'' states. As inferred from Fig. 12d, the size of the SOC in the range $1.60 < R_{OO} < 1.70$ is considerable (average value of 0.001 eV or 8 cm^{-1}). We should mention that at some specific geometries, (namely $R_{OO} \sim 1.64$ and $100 \leq \theta_{COO} \leq 102.5$), the energy gap between the C^1A' and a^3A'' states is between 0.5–0.6 eV (see Fig. 12b), where the size of SOC is considerable. Thus, in this case one would expect to have a moderately efficient ISC process, but it is not as efficient as for the case of the B^1A' and a^3A'' states. In Fig. 13, the contour plots of the energy differences between the 2D PESs for the (B^1A', b^3A'') and (C^1A', b^3A'') are shown. In Fig. 13c and d, the size of SOC matrix elements at the geometries close to the (B^1A', b^3A'') and (C^1A', b^3A'') avoided crossing are shown, respectively. In general, Fig. 13 indicates that the size of SOC matrix elements are not large enough at the avoided crossing geometries, where the energy gap is small. Thus, we do not expect an efficient ISC crossing to occur between the (B^1A', b^3A'') and (C^1A', b^3A'') states.

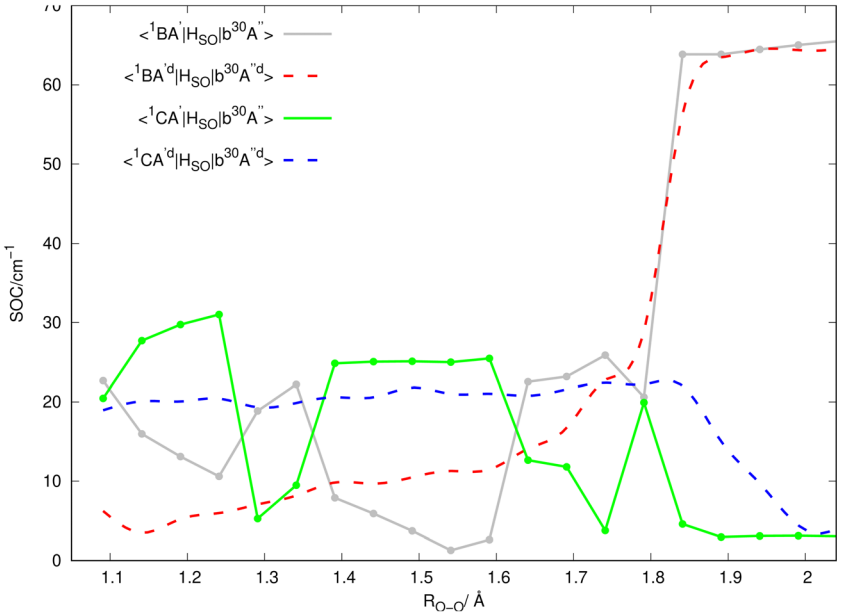

Fig. 11 SOC matrix elements (shown in the caption of the figure) in the adiabatic (solid lines) and diabatic (dashed lines) representations.

As a result of the aforementioned reasoning, one may conclude that the ISC mechanism is more likely to happen between the two states B^1A' and a^3A''. This finding is also consistent with the El-Sayed rule indicating that the rate of intersystem crossing is relatively large if the radiationless transition involves a change of orbital type.[16,17] Based on this

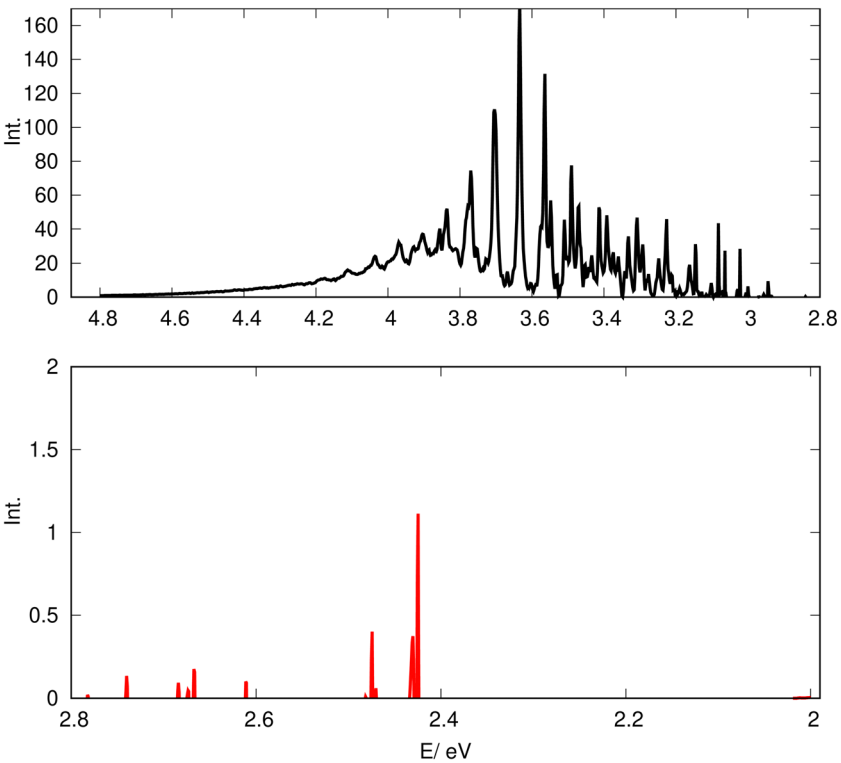

Fig. 12 (a) The energy difference (in eV) between the PESs of the B^1A' and a^3A'' states along the R_{OO} and θ_{COO} coordinates. (b) The energy difference between the PESs of the C^1A' and a^3A'' states along the R_{OO} and θ_{COO} coordinates. (c) The size of SOC at the geometries close to the B^1A' and $a^{3+}A''$ avoided crossing. The corresponding average value is 0.005 eV (42 cm^{-1}). (d) The size of SOC at the geometries close to the C^1A' and $a^{3+}A''$ avoided crossing. The corresponding average value is 0.001 eV (8 cm^{-1}).

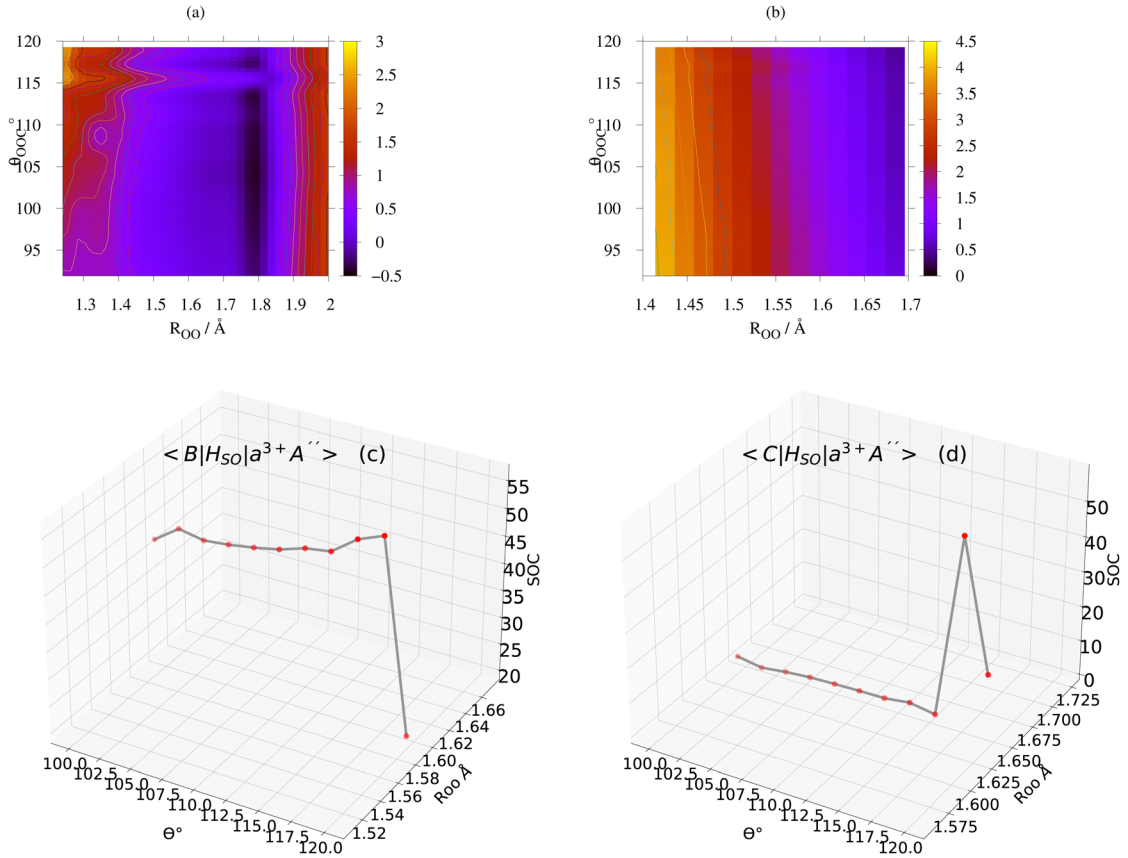

Fig. 13 (a) The energy difference between the PESs (in eV) of the B^1A' and b^3A'' states along the R_{OO} and θ_{COO} coordinates. (b) The energy difference between the PESs of the C^1A' and b^3A'' states along the R_{OO} and θ_{COO} coordinates. (c) The size of SOC at the geometries close to the B^1A' and $b^{3+}A''$ avoided crossing. The corresponding average value is 0.001 eV (8 cm^{-1}). (d) The size of SOC at the geometries close to the C^1A' and $b^{3+}A''$ avoided crossing. The corresponding average value is 0.005 eV (42 cm^{-1}).

Table 1 The minimum and barrier energies of PE curves of the diabatic states B^1A' and $a^{3-}A''$ as shown in Fig. 4

Diabatic states	$E_{min.}$	$E_{barr.}$	Barr. height
B^1A'	3.00	3.44	0.44
a^3A''	2.35	3.09	0.74

rule, the mixing between the $B^1A'(^1\pi\pi^*)$ and $a^3A''(^3n\pi^*)$ states is allowed to occur *via* SOC, because these states have different orbital characters.

5 Dynamics

5.1 Excitation spectrum

For the evaluation of the spectrum, we perform a propagation calculation using the Hamiltonian model of eqn (2) with a time step 0.05 fs for 1000 fs. This follows after lifting the initial wavepacket from the ground X to the excited B state. The initial wavepacket is computed *via* propagation in imaginary time by employing the ground state PES of CH_2OO.[41,42] The method is known as relaxation technique not only in the MCTDH formalism, but quite generally.[42–45] In the MCTDH wavepacket propagation,[42–45] one needs to choose an appropriate DVR, which yields an efficient and accurate form of the wavefunction Ψ. In this work, we choose the harmonic oscillator (HO) DVR and fast Fourier transform (FFT) in the propagation.[42,45] In Table 2, we list the size of the primitive basis and number of single particle functions (SPFs) employed in the current work.

Table 2 Number of basis functions for the primitive harmonic and SPF basis used for the MCTDH calculation. The ordering of the SPF basis for the states involved in the dynamics is the X^1A', a^3A', b^3A', a^3A'', b^3A'', B^1A' and C^1A' states

Modes	DVR	Primitive basis	SPF basis
R_{OO}	FFT	128	9, 10, 9, 9, 9, 9, 9
R_{CO}	HO	88	9, 10, 9, 9, 9, 9, 9
θ_{COO}	HO	80	9, 10, 9, 9, 9, 9, 9

Since we study the photodissociation process *via* the O–O bond cleavage, the wavepacket can be reflected, or it penetrates the other side of the grid when periodic boundary conditions (*e.g.* FFT) are employed. This leads to the depreciation of the wavefunction. As stated by Leforestier and Wyatt,[46] and later Kosloff,[47] one uses a complex absorbing potential (CAP) along the O–O stretching mode to avoid the convergence issue in the

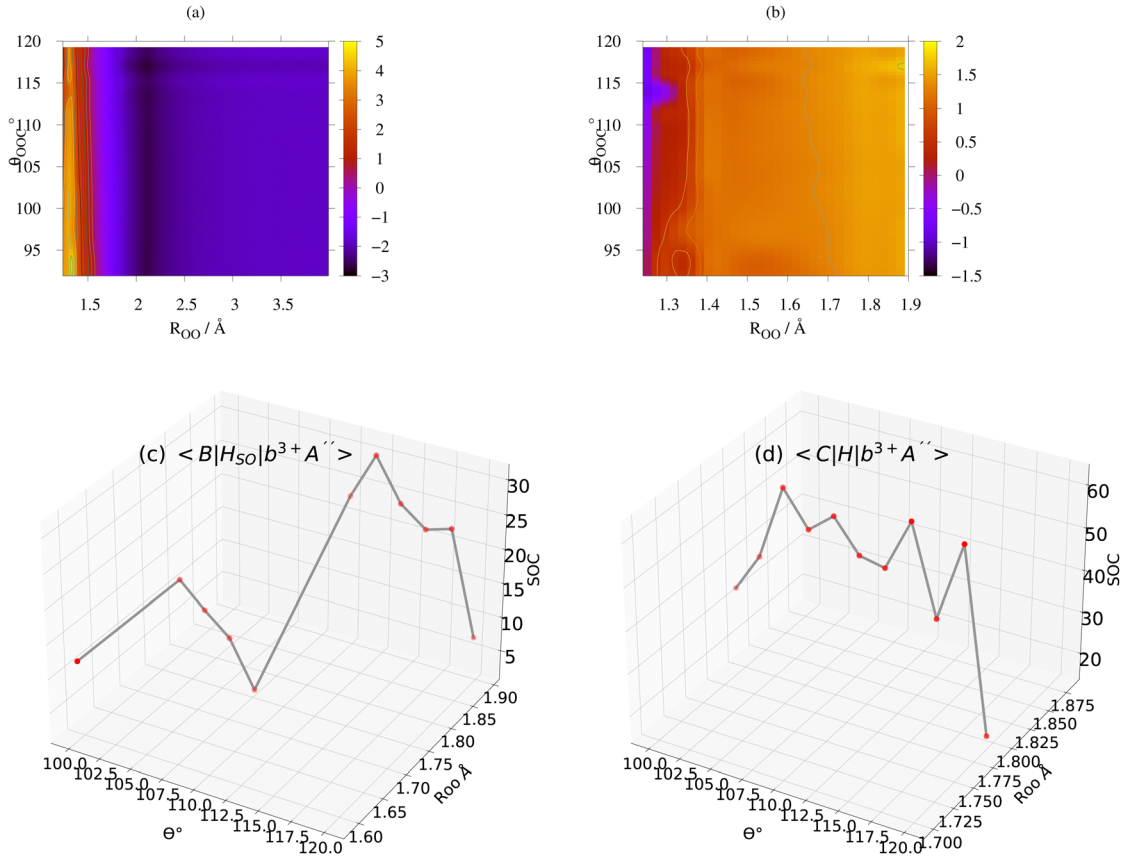

Fig. 14 The excitation spectrum of CH_2OO computed by the model Hamiltonian in eqn (1) with the coupled singlet and triplet states. For the evaluation of the spectrum, the average values of SOC matrix elements at the geometries close to the avoided crossing (see Fig. 12 and 13) are used. The upper panel (black color) is the spectral band corresponding to the $B^1A' \leftarrow X^1A'$ transition, while the lower panel spectrum (red color) is the spectral band caused by the triplet states and SOCs. The oneset of the $B^1A' \leftarrow X^1A'$ spectral band is above the minimum energy of 3D PESs of B^1A' (E_{min} = 2.41 eV). The onset of the spectrum in the lower panel is above the minimum energy of 3D PESs of a^3A' (E_{min} = 1.45 eV) and below the barrier energy of a^3A'' (3.09 eV) as shown in Fig. 4 and Table 1.

WP propagation. The CAP is a negative imaginary potential used to absorb the wavepacket as it approaches the end of the grid and thus helps the propagation to converge better along the O–O stretching coordinate. The CAP is usually defined as follows[42]

$$iW(Q) = -i\eta(Q - Q_c)^b\theta(Q - Q_c) \quad (19)$$

In this equation, Q_c, b and η are the starting point, order, and strength of the CAP, respectively. The parameters Q_c, b and η used in the current work are 2.1 Å, 3.1×10^{-4} a.u., 3, respectively. The symbol $\theta(x)$ denotes Heaviside's step function. The distance between the starting point of the CAP and the end of the grid determines the length of the CAP, which is usually determined by visualizing the topology of potential energy cuts. The optimal CAP order is 2 or 3 as suggested in ref. 48. In our study, the length of CAP is ~1 Å resulting in a smaller CAP strength η to produce unwanted CAP reflections in the quantum dynamical calculation (see ref. 48 for more information for determining the CAP parameters). We thus modify the potential part of the Hamiltonian in eqn (2) by adding $iW(Q)$ according to eqn (20).

In Fig. 14, we present the computed spectrum for the different energy ranges. In the upper panel of Fig. 14, the spectral band with an energy larger than 2.8 eV (black color) corresponding to the $B^1A' \leftarrow X^1A'$ transition is shown. This part of the spectrum is in excellent agreement with the experiment[28,29] as also shown in our previous work.[26] In the lower panel, the spectrum in the energy range below 2.8 eV, shown by the red color, represents the spectral band, in which the contributions of the two lowest triplet states with a^3A' and a^3A'' symmetry including their SOCs with the B^1A' and C^1A' states (see eqn (2)) play a role. This spectral band showing an irregular and discrete structure is ~0.9 eV above the minimum energy of the 3D PESs of a^3A' (E_{min} = 1.45 eV). This spectral band is below the energy barrier of the a^3A'' state (3.09 eV) as shown in Table 1 and Fig. 4. As can be seen from Fig. 4, the barrier height of a^3A'' state (0.74 eV) is larger than the one in B^1A' (0.44 eV) indicated explicitly in Fig. 4. Due to this deeper well of the diabatic state a^3A'' at R_{OO} = 1.791 Å, (which is below the starting point of the CAP at Q_c = 2.1 shown by the green dashed-dotted line in Fig. 4), the wavepackets corresponding to the $a^{3+}A''$ and $a^{30}A''$ states as shown in Fig. 17 are partly reflected by the barrier to the right of the shallow well at R_{OO} = 1.791 Å (shown in Fig. 4) resulting in the discrete structure. The intensity of the triplet band in the lower panel in Fig. 14 is considerably smaller than that of the singlet band in the upper panel. The intensity ratio between the highest peaks of the triplet and singlet bands is

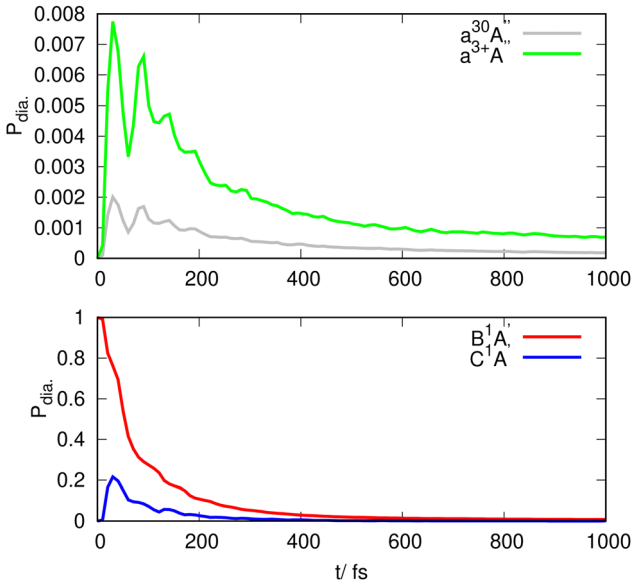

Fig. 15 The diabatic electronic populations of the singlet and triplet states involved in the dynamics of CH_2OO following excitation to the B state. For more details see the text.

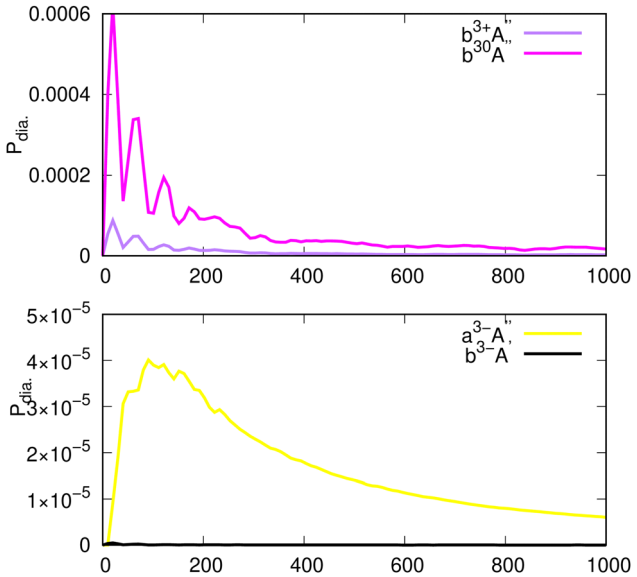

Fig. 16 The diabatic electronic populations of the triplet states involved in the dynamics of CH_2OO following excitation to the B state. For more details see the text.

$\sim$0.006. This small intensity of the triplet band is expected, which is due to the average value of SOC between the B^1A' and a^3A'' (0.005 eV, see Fig. 12c).

5.2 Time-dependent population analysis

This section is devoted to the study of the time-dependent populations $P_\alpha(t)$ of the electronic states α involved in the photodissociation dynamics of CH_2OO. $P_\alpha(t)$ is computed *via* $\langle\Psi_\alpha(t)|\Psi_\alpha(t)\rangle$, where $\Psi_\alpha(t)$ is the propagated wavefunction (for the method of computing $|\Psi_\alpha(t)\rangle$ see ref. 42 and 43). In Fig. 15 and 16, the diabatic electronic populations of the singlet and triplet sates considering their spin components are shown. In the lower panel of Fig. 15, the diabatic populations of the B^1A' and C^1A' states are depicted. At $t = 0$, the system is in the B state due to the fact that the initial wavefunction is lifted from the X^1A' to the B^1A' state. Within the propagation time, while the B state population decreases relatively fast within the lifetime τ = 74 fs (obtained *via* fitting $ae^{-t/\tau}$ to the population of the B state), the C state population has a moderate increase at t = 50 fs. For the later propagation times $t \gg 50$ fs, the populations decrease less than $\sim$0.001. In the upper panel of Fig. 15, the populations of the states $a^{3+}A''$ and $a^{30}A''$ are shown. The population of $a^{3+}A''$ (the green line) has a relatively sharp increase until $t \sim 50$ fs and thereafter, it oscillates and decreases very slowly until the end of the propagation time at 1000 fs. In this figure, the population of $a^{30}A''$ (the gray line) is shown representing a similar behavior compared to the population of $a^{3+}A''$ state but with less enhancement in its population at t = 50 fs. In Fig. 16, the populations of other triplet states are also shown. It can be seen that amount population transfer from the diabatic populations of states depicted in Fig. 15 to the states in Fig. 16 is small.

For a better understanding, Fig. 17 shows WP snapshots (reduced densities) for the B^1A', $a^{3+}A''$ and $a^{30}A''$ states for the selected propagation times given in the legend of the figure. For both states, the WP moves to the right (larger O–O distances) and broadens, (especially in the case of the $a^{3+}A''$ and $a^{30}A''$ states). The $a^{3+}A''$ population oscillates and decreases as depicted by Fig. 15 and this is due to the fact that the WP is moving towards and within the range of the CAP, see green dashed line in Fig. 4. Strictly speaking, the WP gets partly reflected within the deep shallow well corresponding to the $a^{3+}A''$ near 1.791 Å, which causes the discrete structure in the spectrum in the lower panel of Fig. 14. The parts moving out are suppressed by the CAP and the population decreases which represents photodissociation of CH_2OO into the $H_2CO(X^1A_1)$ and O^3P products.

It can be seen that there is a population transfer from the B to the relevant triplet states, which cannot be ignored, especially there is a considerable transfer to the $a^{3+}A''$ and $a^{30}A''$ states (see the upper panel of Fig. 15). This considerable amount of population transfer to the $a^{3+}A''$ and $a^{30}A''$ states seems to be realistic. This can be understood by using the results provided in Fig. 12a and c, showing a sizable SOC at the geometries close to the avoided crossings between the B^1A' to the a^3A'' state. Due to this considerable SOC at those specific geometries, we observe a population transfer from the B^1A' to $a^{3+}A''$ states. This considerable population transfer between these two states represents the role of SOC in the dynamics, which eventually allows for an efficient ISC between the B^1A' and a^3A'' states and provides a path for a spin-forbidden dissociation channel as shown in Fig. 3.

While the population transfer between B^1A' and C^1A' is due to the presence of vibronic coupling W_{BC} (see eqn (2)), the SOCs play a dominant role for transferring the population

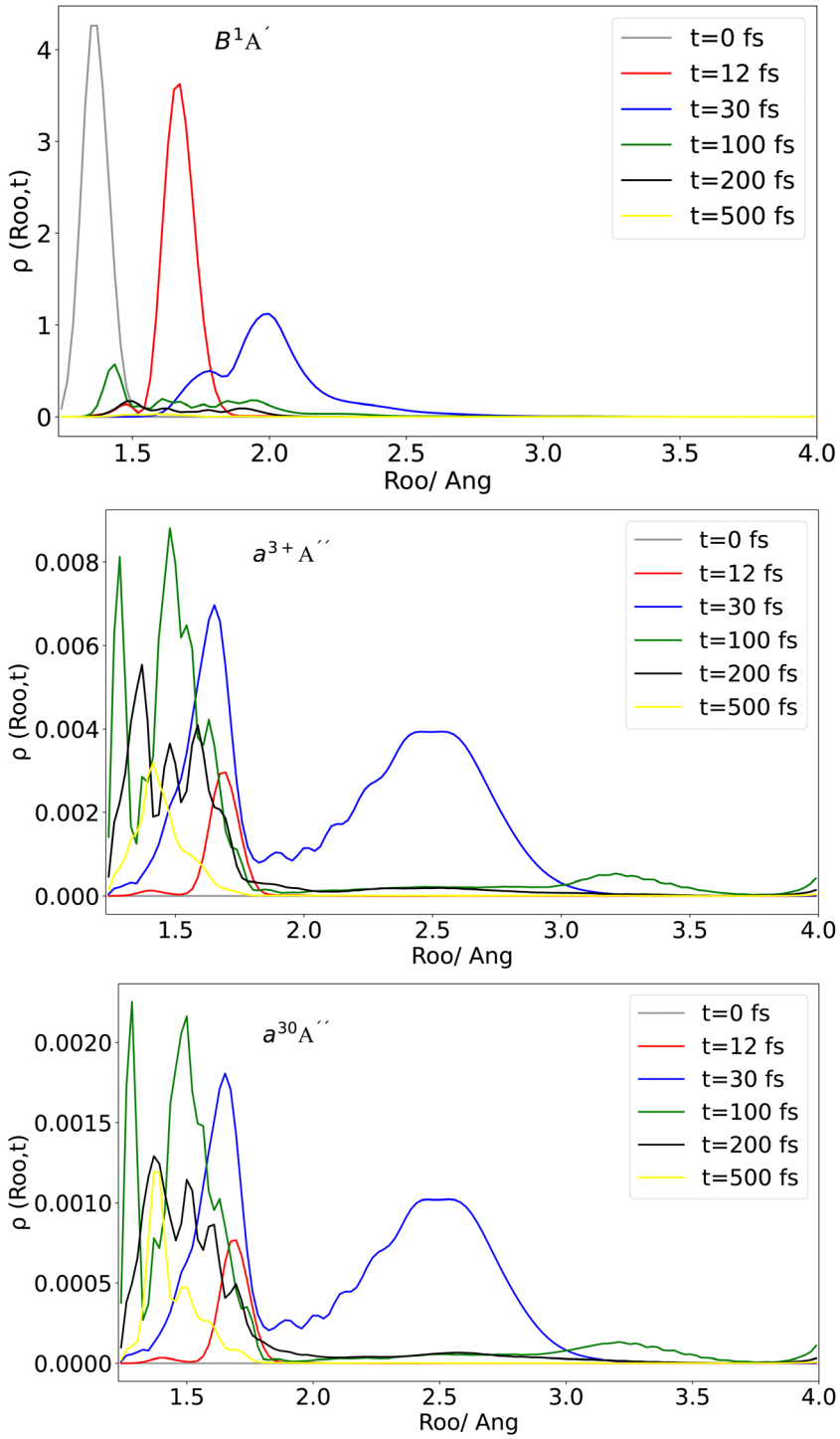

Fig. 17 One-dimensional reduced densities for the B^1A', $a^{3+}A''$ and $a^{30}A''$ states along the OO stretching mode.

between the B^1A' to the a^3A'' state as mentioned above. Due to the weakly avoided crossing of the PE curves of the singlet and triplet states, the fast population transfer occurs within the time scale of 50–100 fs. However, we can observe a small population transfer in the triplet manifold due to the small value for the SOC (0.01 eV), which is related to the small intensity ratio of the triplet and singlet spectra (0.006) mentioned in Section 5.1. We can conclude that both vibronic coupling and SOC are essential for understanding of dynamics. In fact, the later one can be used for understanding another dissociation channel for CH_2OO occurring *via* the ISC mechanism in CH_2OO (see below).

Based on the theoretical considerations provided above, we suggest a photodissociation channel for CH_2OO relying on the triplet states a^3A'' and a^3A' as well as the ISC between B^1A' and a^3A'' as shown schematically in Fig. 2; the UV absorption

process excites CH_2OO from its ground state to the excited state B^1A'. The SOC can mix the $B^1A'(^1\pi\pi^*)$ and $a^3A''(^3n\pi^*)$ based on the El-Sayed's rule. In fact, this mixing originates from the sizable SOC between the B^1A' and a^3A'' states (as shown in Fig. 12a and c) at the geometries close to the avoided crossing. Due to vibronic interaction between the two triplet states a^3A'' and a^3A' (as a result of the avoided crossings between the triplet states shown in Fig. 3 and the vibronic terms of $W_{a'b'}$ and $W_{a''b''}$ in eqn (2)), the molecule relaxes to the a^3A' state and is dissociated into $H_2CO(X^1A_1)$ and O^3P products.

Our findings demonstrate the role of ISC in the (spin-forbidden) dissociation channel of CH_2OO, which has not been addressed fully quantally so far in the literature.[31] This enabled us to treat the excitation spectrum and the electronic populations on an equal footing, a novel step for the Criegee intermediates. Similar findings for other molecular systems with nearly the same size as formaldehyde oxide, such as formaldehyde and acetaldehyde have already been reported in the literature,[49] wherein photodissociation is driven by eventual formation of a triplet state manifold mediated by efficient intersystem crossing from an initially excited bright singlet state. Van veen *et al.* measured the absorption spectra of formaldehyde and acetaldehyde including spectral bands with important contributions from the lowest triplet states and possible SOCs between the singlet and triplet states in these aldehydes.[49]

6 Summary and conclusion

In this article we have presented a unified Hamiltonian model, in which the contributions of the SOC and vibronic couplings for describing the photodissociation dynamics of CH_2OO *via* the two dissociation channels $H_2CO(X^1A_1)$ + O^1D and $H_2CO(X^1A_1)$ + O^3P are taken into account and treated on an equal footing. Contributions PESs of triplet states with different spin components M_s = 0, ±1 and their spin–orbit couplings with the other singlet states B and C are explicitly taken into account in our calculation. This is a novel step in the theoretical treatment of the photodynamics of the Criegee intermediates. The PESs and SOCs are computed using the RS2-F12 method and MRCI wavefunction, respectively. The ATD angles obtained from the diabatization of the three sets of the coupled states (B^1A',C^1A'), (a^3A',b^3A') and (a^3A'',b^3A'') lead to the diabatizations of the relevant SOC matrix elements and remove the discontinuities in the PESs and SOCs as function of the O–O stretching coordinate. Combining a perturbative explicit-correlation treatment for the electronic motion with a fully quantal approach for the fifteen coupled PESs (*via* vibronic and SOC couplings) enabled us to compute the spectral band generated due to the presence of SOCs, which is located below the onset of the $B^1A' \leftarrow X^1A'$ absorption spectrum. This in turn shows that both vibronic and SOC couplings need to be considered to properly describe the photodissociation dynamics of CH_2OO. The population transfer between B^1A' and a^3A'' occurring during the propagation time is indicative of the efficient ISC process between these two states and hence, the dissociation CH_2OO into the $H_2CO(X^1A_1)$ and O^3P products.

Data availability

The data that support the findings of this study are available based on a reasonable request from authors.

Conflicts of interest

There are no conflicts to declare.

Acknowledgements

We are indebted to the Deutsche Forschungsgemeinschaft (DFG) for financial support (KO 945/22-1). The authors acknowledge support by the state of Baden-Württemberg through bwHPC (JUSTUS 2 cluster).

Notes and references

1 R. S. Minns, D. S. N. Parker, T. J. Penfold, G. A. Worth and H. H. Fielding, *Phys. Chem. Chem. Phys.*, 2010, **12**, 15607–15615.
2 M. Richter, P. Marquetand, J. González-Vázquez, I. Sola and L. González, *J. Phys. Chem. Lett.*, 2012, **3**, 3090–3095.
3 M. Richter, S. Mai, P. Marquetand and L. González, *Phys. Chem. Chem. Phys.*, 2014, **16**, 24423–24436.
4 A. Sidat, F. J. Hernández, L. Stojanović, A. J. Misquitta and R. Crespo-Otero, *Phys. Chem. Chem. Phys.*, 2022, **24**, 29437–29450.
5 B. F. E. Curchod, C. Rauer, P. Marquetand, L. González and T. J. Martínez, *J. Chem. Phys.*, 2016, **144**, 101102.
6 B. Nikoobakht and H. Köppel, *Chem. Phys. Lett.*, 2016, **651**, 221–232.
7 T. J. Penfold, E. Gindensperger, C. Daniel and C. M. Marian, *Chem. Rev.*, 2018, **118**, 6975–7025.
8 W. Domcke, D. R. Yarkony and H. Köppel, *Conical Intersections: Electronic Structure, Dynamics and Spectroscopy*, World Scientific, New Jersey, 2004.
9 H. Köppel, W. Domcke and L. S. Cederbaum, *Adv. Chem. Phys.*, 1984, **57**, 59–246.
10 S. Fernandez-Alberti, A. E. Roitberg, T. Nelson and S. Tretiak, *J. Chem. Phys.*, 2012, **137**, 014512.
11 J. P. Heritage and A. Penzkofer, *Chem. Phys. Lett.*, 1976, **44**, 76–81.
12 M. A. El-Sayed, *J. Chem. Phys.*, 1962, **36**, 573–574.
13 M. A. El-Sayed, *J. Chem. Phys.*, 1964, **41**, 2462–2467.
14 C.-H. Ting, *Photochem. Photobiol.*, 1969, **9**, 17–31.
15 N. J. Turro, V. Ramamurthy and J. C. Scaiano, *Principles of Molecular Photochemistry: An Introduction*, University Science Books, Sausalito, California, 1945.
16 M. A. El-Sayed, *J. Chem. Phys.*, 1963, **38**, 2834–2838.
17 S. K. Lower and M. A. El-Sayed, *Chem. Rev.*, 1966, **66**, 199.

18 A. Thiel and H. Köppel, *J. Chem. Phys.*, 1999, **110**, 9371–9383.
19 H. Köppel, J. Gronki and S. Mahapatra, *J. Chem. Phys.*, 2001, **115**, 2377–2388.
20 T. Shiozaki and H.-J. Werner, *J. Chem. Phys.*, 2011, **134**, 184104.
21 T. Shiozaki and H.-J. Werner, *J. Chem. Phys.*, 2010, **133**, 141103.
22 P. Aplincourt, E. Henon, F. Bohr and M. Ruiz-López, *Chem. Phys.*, 2002, **285**, 221–231.
23 M. T. Nguyen, T. L. Nguyen, V. T. Ngan and H. M. T. Nguyen, *Chem. Phys. Lett.*, 2007, **448**, 183–188.
24 M. C. McCarthy, L. Cheng, K. N. Crabtree, O. Martinez, T. L. Nguyen, C. C. Womack and J. F. Stanton, *J. Phys. Chem. Lett.*, 2013, **4**, 4133–4139.
25 B. Nikoobakht and H. Köppel, *Mol. Phys.*, 2021, e1958019.
26 B. Nikoobakht and H. Köppel, *Phys. Chem. Chem. Phys.*, 2022, **24**, 12433–12441.
27 L. Sheps, *J. Phys. Chem. Lett.*, 2013, **4**, 4201–4205.
28 W.-L. Ting, Y.-H. Chen, W. Chao, M. C. Smith and J. J.-M. Lin, *Phys. Chem. Chem. Phys.*, 2014, **16**, 10438–10443.
29 E. S. Foreman, K. M. Kapnas, Y. Jou, J. Kalinowski, D. Feng, R. B. Gerber and C. Murray, *Phys. Chem. Chem. Phys.*, 2015, **17**, 32539–32546.
30 J. H. Lehman, H. Li, J. M. Beames and M. I. Lester, *J. Chem. Phys.*, 2013, **139**, 141103.
31 V. J. Esposito, O. Werba, S. A. Bush, B. Marchetti and T. N. V. Karsili, *Photochem. Photobiol.*, 2022, **98**, 763–772.
32 E. B. Wilson, J. C. Decius and P. Cross, *Molecular vibrations: the theory of infrared and Raman vibrational spectra*, McGraw-Hill, New York City, 1955.
33 E. B. Wilson, *J. Chem. Phys.*, 1939, **7**, 1047–1052.
34 Horst Köppel, Unpublished results (2024).
35 G. Knizia, T. B. Adler and H.-J. Werner, *J. Chem. Phys.*, 2009, **130**, 054104.
36 T. H. Dunning, *J. Chem. Phys.*, 1989, **90**, 1007–1023.
37 Y. Guan, H. Guo and D. R. Yarkony, *J. Chem. Theory Comput.*, 2020, **16**, 302–313.
38 A. Berning, M. Schweizer, H.-J. Werner, P. J. Knowles and P. Palmieri, *Mol. Phys.*, 2000, **98**, 1823–1833.
39 H.-J. Werner and P. Knowles, *MOLPRO, version 2019.2, a package of ab initio programs*, 2019, For the current version, see **https://www.molpro.net/**.
40 H. Li, Y. Fang, J. M. Beames and M. I. Lester, *J. Chem. Phys.*, 2015, **142**, 214312.
41 R. Kosloff and H. Tal-Ezer, *Chem. Phys. Lett.*, 1986, **127**, 223–230.
42 M. Beck, A. Jäckle, G. Worth and H.-D. Meyer, *Phys. Rep.*, 2000, **324**, 1–105.
43 H.-D. Meyer, U. Manthe and L. S. Cederbaum, *Chem. Phys. Lett.*, 1990, **165**, 73–78.
44 M. Beck, A. Jäckle, G. Worth and H.-D. Meyer, *MCTDH, The Heidelberg MCTDH Package Version 8.4.20, For the current version*, see **https://www.pci.uni-heidelberg.de/tc/usr/mctdh/doc/index.html**.
45 H.-D. Meyer, F. Gatti and G. Worth, *Multidimensional Quantum Dynamics: MCTDH Theory and Applications*, Wiley-VCH Verlag GmbH and Co. KGaA, Weinheim, 2009.
46 C. Leforestier and R. E. Wyatt, *J. Chem. Phys.*, 1983, **78**, 2334–2344.
47 R. Kosloff and D. D. Kosloff, *J. Comput. Phys.*, 1986, **63**, 363–376.
48 U. V. Riss and H.-D. Meyer, *J. Chem. Phys.*, 1996, **105**, 1409–1419.
49 E. H. van Veen, W. L. van Dijk and H. H. Brongersma, *Chem. Phys.*, 1976, **16**, 337–345.

